analytical chemistry

pubs.acs.org/ac Letter

Near-Infrared Light-Induced Self-Powered Aptasensing Platform for Aflatoxin B1 Based on Upconversion Nanoparticles-Doped Bi_2S_3 Nanorods

Jie Gao, Xiaoling Yao, Yingxu Chen, Zhonghong Gao, and Jingdong Zhang*

Cite This: https://dx.doi.org/10.1021/acs.analchem.0c04248 Read Online

ACCESS | Metrics & More | Article Recommendations | Supporting Information

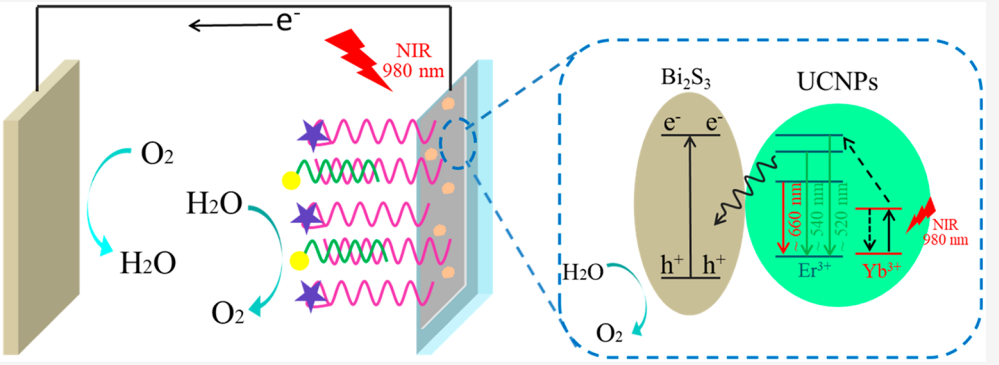

ABSTRACT: A light source plays a pivotal role in a photofuel cell (PFC)-based self-powered biosensor. Although a visible light source has been extensively employed to drive a PFC, it still has some drawbacks for biosensing due to its relatively high energy. Herein we constructed a PFC-based aptasensor using near-infrared (NIR) light as the irradiation source. To achieve an efficient absorption of the NIR light, $NaYF_4$:Yb,Er upconversion nanoparticles (UCNPs) that could convert low-energy incident light into high-energy radiation were combined with Bi_2S_3 nanorods (UCNPs/Bi_2S_3) to serve as the photoactive materials. The PFC was comprised of a UCNPs/Bi_2S_3 photoanode and a Pt cathode, which could generate electrical output under NIR light irradiation to provide the self-powered sensing signal without the supply from an external power source. The aflatoxin B1 (AFB1) binding aptamer was immobilized on the photoanode to serve as the recognition element. The detection of AFB1 was based on the competition between the interaction of aptamer with AFB1 analyte and the hybridization of aptamer with Au nanoparticles-labeled DNA sequence (AuNPs-cDNA). Under optimum conditions, the proposed aptasensor presented good sensitivity and high specificity for AFB1 detection in the concentration range from 0.01 to 100 ng·mL^{-1}, with a detection limit of 7.9 ng·mL^{-1}. Moreover, the developed sensor was applied to an assay of AFB1 in flour samples with a desirable accuracy and precision.

Fuel-cell-based self-powered sensors have been widely explored for biochemical analysis in the recent decade because of their simpler instrumentation than traditional electrochemical sensors.[1] Since the first enzymatic biofuel cell (EBFC)-based self-powered sensor was realized in 2001, EBFC has been the most common way to construct such sensors;[2] however, it suffers from limited enzyme species and a vulnerability to environmental impact.[3,4] By contrast, a photofuel cell (PFC) based on a highly efficient and stable photocatalyst that can overcome the drawbacks of the enzyme has been deemed as a prospective candidate for the development of self-powered sensors.[5−7] Because the sensitivity of such a sensor is generally dependent upon the output of a PFC, developing highly active photocatalyst plays a crucial role in PFC construction. Moreover, the illumination of the light source directly determines the photon-electron conversion efficiency[8] and thus affects the output power of a PFC. Although UV light has high energy that can activate many photocatalysts to generate a desirable output, it is seldom used as the source for self-powered sensing, because it may damage the biological recognition element or sample.[9] Currently, almost all PFC-based sensors have been proposed under the illumination of visible light, which possesses lower energy than UV light. Moreover, the exploration of visible-light-driven PFC provides the basis for utilization of natural solar light considering that visible light occupies 43% of the solar spectrum.

Received: October 9, 2020
Accepted: November 30, 2020

Actually, a biochemical analysis under near-infrared (NIR) light presents several advantages, such as a large fraction (more than 50%) of the solar spectrum, minimal photobleaching, low phototoxicity, and the elimination of autofluorescence from a biological substance.[10,11] Nevertheless, conventional semiconducting photocatalysts with a relatively fixed bandgap cannot generate effective electron−hole pairs under low-energy NIR light radiation. Upconversion nanoparticles (UCNPs) can convert lower-energy photon radiation into higher-energy output emission via an anti-Stokes optical process.[12−14] In particular, lanthanide-based UCNPs have been widely used in bioimaging,[15,16] photodynamic therapy,[17,18] and other fields due to their large anti-Stokes shift. In particular, the fabrication of a UCNPs/semiconductor composite could broaden the solar-light-harvesting ability of semiconductors. Li et al. prepared UCNPs-Pt@MOF/Au composites, which could be used for photocatalytic hydrogen production under UV, visible, or even NIR irradiation.[19] Tang's group designed a photoelectrochemical enzyme immunoassay based on UCNP@Au@CdS for the ultrasensitive detection of α-fetoprotein.[20] Wang and co-workers reported an NIR-driven photoelectrochemical aptasensor for the detection of breast cancer cell MCF-7.[10] These works demonstrate the feasibility of UCNPs/semiconductor composite as photocatalyst to construct NIR-light-driven sensors.

Aflatoxins are a secondary metabolite produced by *Aspergillus parasiticus* and *Aspergillus flavus*, which has been classified into group I carcinogens. Among the aflatoxins and their derivatives, aflatoxin B1 (AFB1) is one of the most carcinogenic chemical substances known and also the most common one in natural food that is easy to pollute, namely, corn, peanut, and oil made from grain and feed.[21,22] The long-term exposure to AFB1 may lead to terrible diseases such as kidney disorders, immune suppression, cell necrosis, and cancer.[23] Many countries have set the maximum tolerant limit of AFB1. For example, the maximum residue of AFB1 in cereals is 20 ng/mL in China.[24] The European Commission has set a maximum value of AFB1 at 0.5 ng/mL in edible food.[25] Thus, it is of significant importance to develop sensors with high specificity and sensitivity for AFB1 detection to ensure food safety. Xiao et al. designed a UCNPs-based luminescence resonance energy-transfer aptasensor for the quantitative detection of AFB1 in peanut samples by fluorescence.[26] Ren et al. synthesized CdSe/ZnS luminescent quantum dot beads as an immunochromatographic assay (ICA) signal amplification probe for the ultrasensitive detection of AFB1 in maize.[27] Wang's group constructed an electrochemical aptasensor with porous gold nanocages and a fluorescent aptasensor based on the bicolor fluorescence resonance energy transfer from two nanodonors to a single nanoacceptor for AFB1 detection.[28,29] However, these sensors have some drawbacks such as expensive equipment, the need for a skilled person, and harsh experimental conditions.

Herein we propose a novel self-powered aptasensor for the specific detection of AFB1 based on an NIR-light-driven PFC, as illustrated in Scheme 1. We prepared $NaYF_4$:Yb,Er UCNPs-doped Bi_2S_3 (UCNPs/Bi_2S_3) to act as NIR-light-responsive materials (see the Supporting Information for details). The UCNPs/Bi_2S_3 was used to modify an indium tin oxide (ITO) electrode, and then *N*-(3-dimethylaminopropyl)-*N*′-ethylcarbodiimide hydrochloride (EDC) and *N*-hydroxysuccinimide (NHS) were incubated on the electrode to activate the carboxyl group for binding the aminated AFB1 aptamer by a

Scheme 1. Schematic Illustration for (A) Photoanode Fabrication and (B) Structure of NIR-Light-Driven PFC Consisting of a Photoanode and a Pt Cathode in a One-Compartment Cell for the Self-Powered Sensing of AFB1

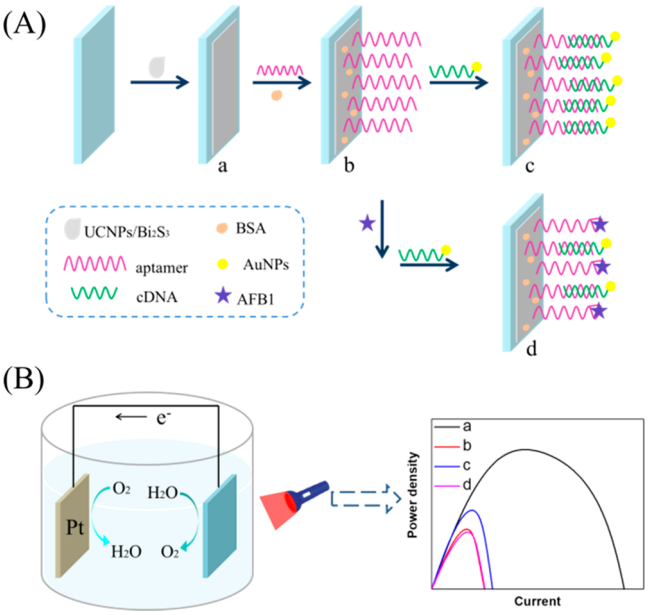

dehydration condensation reaction. The aptamer could hybridize with the Au nanoparticles-labeled DNA sequence (AuNPs-cDNA) through base complementary pairing, which enhanced the output of PFC owing to the excellent electron-transfer ability of AuNPs and the plasma resonance energy transfer (PRET) between AuNPs and UCNPs/Bi_2S_3.[20] While the analyte AFB1 existed, some aptamer molecules interacted with AFB1. As a result, the immobilization amount of AuNPs-cDNA on the electrode via hybridization was reduced, generating a declined output signal of the PFC.

The as-prepared UCNPs/Bi_2S_3 was characterized by scanning electron microscopic (SEM) and X-ray diffraction (XRD) techniques. The SEM observation shows that many homogeneous UCNPs with a size of ca. 40 nm are formed (Figure S1A), while Bi_2S_3 displays a rod-like structure with length in the range from 200 to 500 nm (Figure S1B). In the composite, UCNPs decorated on Bi_2S_3 nanorods can be clearly observed (Figure 1A). According to energy-dispersive spectroscopic (EDS) analysis (Figure S2), the appearance of Na, Y, F, Yb, Er, N, Bi, and S elements further demonstrates the successful synthesis of the composite. Meanwhile, the XRD pattern of UCNPs (curve (a) in Figure 1B) shows four diffraction peaks at 28.3°, 32.7°, 46.9°, and 55.7°, which can be indexed to the (111), (200), (220), and (311) crystal planes in cubic phase $NaYF_4$ (JCPDS No. 77-2042).[12] The diffraction peaks appearing in the XRD pattern of Bi_2S_3 (curve (b) in Figure 1B) are matched well with those of the known pure Bi_2S_3 orthorhombic phase (JCPDS No. 17-0320).[30] In the XRD pattern of UCNPs/Bi_2S_3 (curve (c) in Figure 1B), all the characteristic diffraction peaks of Bi_2S_3 can be identified. Besides, two characteristic diffraction peaks of UCNPs at 28.3° and 55.7° are observed in the enlarged regions in the XRD pattern of UCNPs/Bi_2S_3 (Figure S3), confirming the successful combination of UCNPs and Bi_2S_3. The relatively weak diffraction intensities of UCNPs should be due to only a small portion of UCNPs in the composite.

https://dx.doi.org/10.1021/acs.analchem.0c04248
Anal. Chem. XXXX, XXX, XXX−XXX

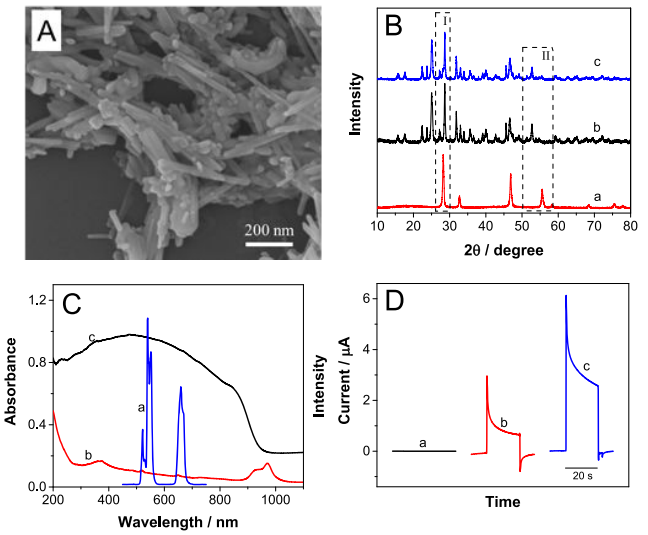

Figure 1. (A) SEM image of UCNPs/Bi_2S_3. (B) XRD patterns of (a) UCNPs, (b) Bi_2S_3, and (c) UCNPs/Bi_2S_3. (C) (a) Upconversion luminescence spectrum of UCNPs and UV−vis−NIR diffuse reflectance spectra of (b) UCNPs and (c) Bi_2S_3. (D) Photocurrent responses of (a) UCNPs/ITO, (b) Bi_2S_3/ITO, and (c) UCNPs/Bi_2S_3/ITO recorded in 0.1 M Na_2SO_4.

To reveal whether the upconversion luminescence of UCNPs could be absorbed by Bi_2S_3, the fluorescence spectrum of UCNPs was first measured under NIR light irradiation with a 980 nm laser. As can be seen, three strong emission peaks of Er^{3+} at 520, 540, and 660 nm appear (curve (a) in Figure 1C), which are assigned to the radioactive transitions of $^2H_{11/2} \rightarrow {}^4I_{15/2}$, $^4S_{3/2} \rightarrow {}^4I_{15/2}$, and $^4F_{9/2} \rightarrow {}^4I_{15/2}$, while Yb^{3+} serves as a sensitizer to absorb the incident light.[31] While UCNPs are doped in Bi_2S_3, the intensities of all the fluorescence peaks decrease significantly (Figure S4A), which may be attributed to the absorption of photon energy from the upconversion process by Bi_2S_3 or reduced NIR excitation intensity reaching on the surfaces of UCNPs by the hindrance of Bi_2S_3.[9,12] Nevertheless, the fluorescence lifetime of UCNPs measured at the emission wavelength of 540 nm is not changed after being combined with Bi_2S_3 (Figure S4B), suggesting that the formation of UCNPs/Bi_2S_3 composite does not affect the upconversion luminescence performance. The UV−vis−NIR diffuse reflectance spectrum (DRS) of UCNPs shows an absorption band around 980 nm (curve (b) in Figure 1C), which is a characteristic of Yb^{3+}. The result confirms that UCNPs can absorb NIR light and convert it to higher-energy light. The DRS of Bi_2S_3 exhibits wide absorption from 300 to 800 nm with stronger absorption around 500 nm (curve (c) in Figure 1C), which overlaps with the emission peaks of UCNPs. Therefore, in the UCNPs/Bi_2S_3 composite, UCNPs are the energy donor, while Bi_2S_3 is the energy receptor, and Bi_2S_3 can receive more energy from the emission of UCNPs under NIR light irradiation to generate more electron−hole pairs.

Figure 1D shows the photocurrent responses of various modified electrodes recorded at a bias potential of 0 V under NIR light irradiation. There is no observable photocurrent on UCNPs modified ITO electrode (curve (a) in Figure 1D). By contrast, Bi_2S_3 modified electrode exhibits a weak photocurrent response (curve (b) in Figure 1D). While the ITO electrode is modified with UCNPs/Bi_2S_3 (curve (c) in Figure 1D), the photocurrent is nearly 4 times that of Bi_2S_3/ITO. These results confirm that, although UCNPs cannot be directly excited by NIR light to generate electron−hole pairs, the upconversion luminescence property of UCNPs absorbed by Bi_2S_3 can effectively improve the NIR light activity of materials. Thus, a UCNPs/Bi_2S_3 modified electrode was employed as the photoanode of a NIR-light-driven PFC in the following study.

The immobilization of the AFB1 aptamer on the UCNPs/Bi_2S_3 modified electrode was studied by an electrochemical impedance spectroscopic (EIS) technique using an $[Fe(CN)_6]^{3-/4-}$ redox probe. The electron-transfer resistance (R_{et}) value of the modified electrode is estimated based on the semicircular diameter of the Nyquist plot.[32] As can be seen, the R_{et} value of the UCNPs/Bi_2S_3 modified electrode is 58.3 Ω (curve (a) in Figure S5). After the AFB1 aptamer is immobilized on UCNPs/Bi_2S_3/ITO, the R_{et} value increases to 114.3 Ω (curve (b) in Figure S5), meaning that the aptamer on the surface of UCNPs/Bi_2S_3 modified electrode increases the steric resistance of the electrode surface. When AuNPs-cDNA is hybridized with the aptamer-immobilized electrode, the R_{et} value decreases to 80.5 Ω (curve (c) in Figure S5). This is owing to the fact AuNPs can act as an electron conduction tunnel to facilitate the electron transfer between the electrode and the redox species.[33] While AFB1 is present, the R_{et} value increases to 92.5 Ω after AFB1 is captured by the aptamer on the modified electrode (curve (d) in Figure S5), manifesting the formation of aptamer−AFB1 complex, which can increase the steric hindrance on the electrode surface.

The polarization curves of the UCNPs/Bi_2S_3 photoanode and Pt cathode were analyzed to study the thermodynamic feasibility of designed PFC. For the UCNPs/Bi_2S_3 photoanode, the onset oxidation potential of H_2O is −0.10 V in the dark (curve (a) in Figure 2A), which decreases slightly to ca. −0.19 V under NIR-light illumination (curve (b) in Figure 2A). For the Pt cathode, no reduction peak is observable in N_2-saturated electrolyte (curve (a) in Figure 2B), whereas a strong reduction peak of dissolved oxygen starting at 0.18 V appears

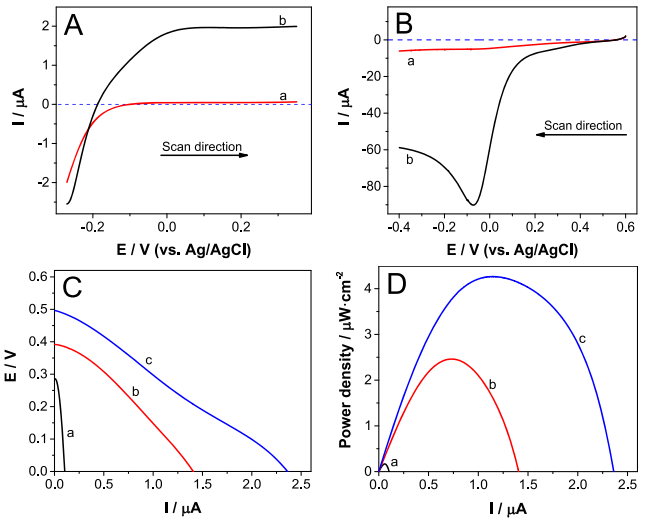

Figure 2. (A) Polarization curves of UCNPs/Bi_2S_3/ITO (a) in the dark and (b) under photoirradiation in 0.1 M Na_2SO_4 at 2 mV/s. (B) Polarization curves of Pt cathode in 0.1 M Na_2SO_4 saturated with (a) N_2 and (b) air at 2 mV/s. (C) *V-I* curves and (D) *P-I* curves of PFCs constructed with Pt cathode and different photoanodes: (a) UCNPs/ITO, (b) Bi_2S_3/ITO, and (c) UCNPs/Bi_2S_3/ITO. The measurements were performed in 0.1 M Na_2SO_4 under NIR-light irradiation.

https://dx.doi.org/10.1021/acs.analchem.0c04248
Anal. Chem. XXXX, XXX, XXX−XXX

in air-saturated electrolyte (curve (b) in Figure 2B). The photoanodic oxidization of H_2O started at a lower potential than the reduction of O_2, meaning the thermodynamic feasibility of the proposed H_2O−O_2 PFC.

The output performances of the proposed PFCs consisting of a Pt cathode and different photoanodes were evaluated by recording the output voltage current (*V-I*) curves and power density-current (*P-I*) curves. As can be seen, under NIR light illumination, both the open-circuit potential (OCP) (Figure 2C) and the maximum output power density (P_{max}) (Figure 2D) of the PFC using UCNPs/Bi_2S_3 photoanode are significantly higher than those of the PFC using either UCNPs or Bi_2S_3 photoanode. The results are in agreement with a high NIR-light activity of UCNPs/Bi_2S_3.

Furthermore, the output performances of PFC using UCNPs/Bi_2S_3 photoanode before and after the immobilization of AFB1 aptamer were compared under photoirradiation to analyze the possibility of the proposed PFC for a self-powered sensing of AFB1. The P_{max} value of the PFC using UCNPs/Bi_2S_3 photoanode is 4.26 $\mu W \cdot cm^{-2}$ (curve (a) in Figure 3A).

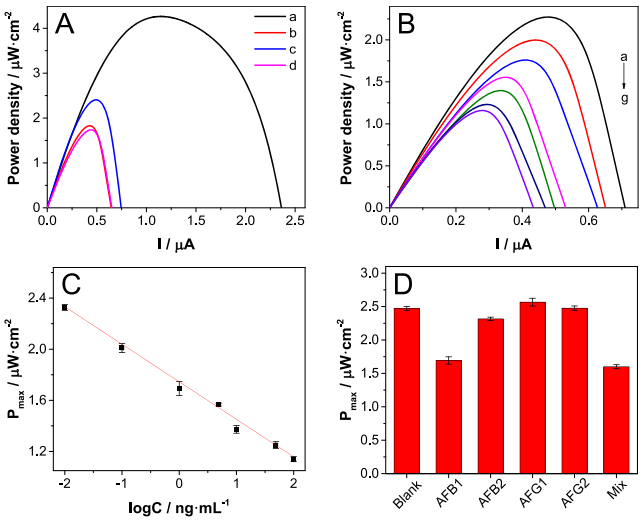

Figure 3. (A) *P*−*I* curves of PFCs constructed with Pt cathode and different photoanodes: (a) UCNPs/Bi_2S_3/ITO, (b) aptamer/UCNPs/Bi_2S_3/ITO, (c) aptamer/UCNPs/Bi_2S_3/ITO incubated with AuNPs-cDNA, (d) aptamer/UCNPs/Bi_2S_3/ITO incubated with AuNPs-cDNA and 1 $ng \cdot mL^{-1}$ AFB1. (B) *P-I* curves of the proposed sensor recorded at different AFB1 concentrations (from (a) to (g)): 0.01, 0.1, 1, 5, 10, 50, and 100 $ng \cdot mL^{-1}$. (C) Calibration curve for AFB1 detection by the proposed sensor. (D) Responses of the proposed sensor toward four toxins (AFB1, AFB2, AFG1, and AFG2) and their mixture (Mix). The concentrations of all the toxins were 1 $ng \cdot mL^{-1}$.

After the aptamer is immobilized on the UCNPs/Bi_2S_3 photoanode, the P_{max} value decreases to 1.82 $\mu W \cdot cm^{-2}$ (curve (b) in Figure 3A), which is attributed to the low conductivity of aptamer, which inhibits the electron-transfer ability of the electrode.[34] While the aptamer is hybridized with AuNPs-cDNA, the P_{max} value increases to 2.44 $\mu W \cdot cm^{-2}$ (curve (c) in Figure 3A) owing to the increased conductivity and the PRET effect of AuNPs. Nevertheless, the P_{max} value declines when the target AFB1 is present (curve (d) in Figure 3A), because the formation of the AFB1−aptamer complex can reduce the binding of AuNPs and increase the steric hindrance for electron transfer. Moreover, a control using a nonfunctional DNA sequence with substituted bases was designed instead of aptamer for testing the PFC response. The results (Figure S6) indicate that the P_{max} of PFC decreases after a nonfunctional DNA sequence is immobilized on the UCNPs/Bi_2S_3 photoanode and then increases after a nonfunctional DNA sequence is hybridized with AuNPs-cDNA, similar to those using aptamer. However, the P_{max} of a nonfunctional DNA sequence/UCNPs/Bi_2S_3/ITO incubated with AuNPs-cDNA in the absence or presence of AFB1 does not show an obvious change. These results indicate that only the aptamer coupled with PFC responding to AFB1 is effective to achieve the self-powered detection.

To achieve the best performance of the developed sensor, the effects of UCNPs content on the photocurrent response of UCNPs/Bi_2S_3 modified electrode and the concentration of aptamer on the output of PFC were investigated. The results (Figure S7) indicated that 15%UCNPs-doped Bi_2S_3 and 1.5 μM aptamer used for fabricating the sensor exhibited the optimum performance for AFB1 detection. Afterward, the calibration curve of AFB1 on the self-powered aptasensor was explored under the optimum conditions. Figure 3B illustrates the *P-I* curves of the fabricated sensor incubated with AFB1 at different concentrations. It is clear that the response of the sensor decreases with the increasing concentration of AFB1. The P_{max} value is found to be linear to the logarithm of AFB1 concentration from 0.01 to 100 $ng \cdot mL^{-1}$ (Figure 3C). The linear regression equation can be expressed as $P_{max}/\mu W \cdot cm^{-2} = -0.2938 \log C/ng \cdot mL^{-1} + 1.7455$, with a correlation coefficient (R^2) of 0.9915. The detection limit (signal-to-noise ratio (S/N) = 3) is calculated to be 7.9 $pg \cdot mL^{-1}$, which is superior to those of many previously reported methods for AFB1 detection (Table S1).

The selectivity of the proposed sensor was evaluated by studying the response of the sensor to AFB1 and other toxins such as aflatoxin B2 (AFB2), aflatoxin G1 (AFG1), and aflatoxin G2 (AFG2). As depicted in Figure 3D, unlike AFB1, all other toxins do not show an obvious influence on the P_{max} value of PFC as compared with the blank solution. Moreover, the P_{max} value of the sensor toward the mixture of AFB2, AFG1, AFG2, and AFB1 is similar to that toward AFB1 only, showing that other three toxins do not cause interference in AFB1 sensing. This result demonstrates that the proposed sensor has a high specificity for AFB1 detection. Besides, the stability of the proposed aptasensor was evaluated by checking the response of the sensor toward 1 $ng \cdot mL^{-1}$ AFB1 every day. The aptamer/UCNPs/Bi_2S_3/ITO electrode was stored at 4 °C when not use. The P_{max} value of the sensor still retains 93.9% of its original response after one week, showing that the sensor possesses a desirable stability.

The self-powered aptasensor was applied to an AFB1 assay in a flour sample using the standard addition method, and the results were compared with those of a commercial enzyme-linked immunosorbent assay (ELISA) kit. The flour was obtained from a local market and pretreated according to a previously reported procedure with a slight modification.[21] Briefly, 5 g of flour sample was immersed in 25 mL of extraction solvent (methanol/water = 5:5 (v/v)). After it was stirred for 1 h, the supernatant was collected via centrifugation at 5000 rpm for 10 min. The sample was diluted 10 times with ultrapure water. Then, a small amount of AFB1 standard solution was spiked into the sample. The content of AFB1 in the flour sample was assayed by the proposed sensor following the self-powered sensing process as described in the

https://dx.doi.org/10.1021/acs.analchem.0c04248
Anal. Chem. XXXX, XXX, XXX−XXX

Supporting Information. As shown in Table S2, the measured results are consistent with the reference values provided by the ELISA kit, and the recovery values are in the range of 97%−110%. These results indicate that this sensor is feasible to be applied to AFB1 detection in real samples.

In conclusion, we have successfully constructed the first NIR-light-driven PFC for the self-powered sensing of AFB1. In the designed PFC, H_2O was oxidized on UCNPs/Bi_2S_3 photoanode under NIR light irradiation, while dissolved oxygen was reduced on a Pt cathode, inducing the generation of electrical output to drive the sensing process. The fabricated self-powered aptasensor for AFB1 exhibited good analytical performances of a wide linear range, low detection limit, and high selectivity. This work expands the PFC irradiation source from visible light to NIR light and offers a new approach to the development of NIR light-responsive biosensing devices for food safety control and environmental analysis.

■ ASSOCIATED CONTENT

Supporting Information

The Supporting Information is available free of charge at https://pubs.acs.org/doi/10.1021/acs.analchem.0c04248.

Additional experimental details, figures showing SEM, EDS mapping results, EIS analysis, sensor optimization, tables showing a comparison of different sensors for AFB1 determination, and feasibility of the sensor in real samples (PDF)

■ AUTHOR INFORMATION

Corresponding Author

Jingdong Zhang − *Key Laboratory of Material Chemistry for Energy Conversion and Storage (Ministry of Education), School of Chemistry and Chemical Engineering, Huazhong University of Science and Technology, Wuhan 430074, P. R. China;* orcid.org/0000-0001-7612-8498; Phone: +86-27-87543032; Email: zhangjd@mail.hust.edu.cn; Fax: +86-27-87543632

Authors

Jie Gao − *Key Laboratory of Material Chemistry for Energy Conversion and Storage (Ministry of Education), School of Chemistry and Chemical Engineering, Huazhong University of Science and Technology, Wuhan 430074, P. R. China*

Xiaoling Yao − *Key Laboratory of Material Chemistry for Energy Conversion and Storage (Ministry of Education), School of Chemistry and Chemical Engineering, Huazhong University of Science and Technology, Wuhan 430074, P. R. China*

Yingxu Chen − *Key Laboratory of Material Chemistry for Energy Conversion and Storage (Ministry of Education), School of Chemistry and Chemical Engineering, Huazhong University of Science and Technology, Wuhan 430074, P. R. China*

Zhonghong Gao − *Key Laboratory of Material Chemistry for Energy Conversion and Storage (Ministry of Education), School of Chemistry and Chemical Engineering, Huazhong University of Science and Technology, Wuhan 430074, P. R. China;* orcid.org/0000-0002-7878-9801

Complete contact information is available at: https://pubs.acs.org/10.1021/acs.analchem.0c04248

Author Contributions

The manuscript was written through contributions of all authors. All authors have given approval to the final version of the manuscript.

Notes

The authors declare no competing financial interest.

■ ACKNOWLEDGMENTS

This work was supported by the Application Foundation Frontier Project of Wuhan Science and Technology Program (Grant No. 2020020601012286), National Natural Science Foundation of China (Grant No. 61571198), and China Postdoctoral Science Foundation (Grant No. 2019M652618). We also thank the Analytical and Testing Center of Huazhong University of Science and Technology for help in materials characterization.

■ REFERENCES

(1) Chen, Y.; Ji, W.; Yan, K.; Gao, J.; Zhang, J. *Nano Energy* **2019**, *61*, 173−193.
(2) Grattieri, M.; Minteer, S. D. *ACS Sens* **2018**, *3*, 44−53.
(3) Huang, L.; Chen, J.; Yu, Z.; Tang, D. *Anal. Chem.* **2020**, *92*, 2809−2814.
(4) Yu, Z.; Cai, G.; Ren, R.; Tang, D. *Analyst* **2018**, *143*, 2992−2996.
(5) Du, X. J.; Jiang, D.; Liu, Q.; Hao, N.; Wang, K. *Anal. Chem.* **2019**, *91*, 1728−1732.
(6) Yan, K.; Zhu, Y.; Ji, W.; Chen, F.; Zhang, J. *Anal. Chem.* **2018**, *90*, 9662−9666.
(7) Ji, W. H.; Yan, K.; Chen, Y. X.; Gao, J.; Zhang, J. D. *Sens. Actuators, B* **2019**, *292*, 129−135.
(8) Shu, J.; Tang, D. *Anal. Chem.* **2020**, *92*, 363−377.
(9) Qiu, Z.; Shu, J.; Tang, D. *Anal. Chem.* **2018**, *90*, 1021−1028.
(10) Wang, K.; Zhang, R.; Sun, N.; Li, X.; Wang, J.; Cao, Y.; Pei, R. *ACS Appl. Mater. Interfaces* **2016**, *8*, 25834−25839.
(11) Luo, Z. B.; Qi, Q. G.; Zhang, L. J.; Zeng, R. J.; Su, L. S.; Tang, D. P. *Anal. Chem.* **2019**, *91*, 4149−4156.
(12) Qiu, Z. L.; Shu, J.; Tang, D. P. *Anal. Chem.* **2018**, *90*, 12214−12220.
(13) Fan, W. Q.; Bai, H. Y.; Shi, W. D. *CrystEngComm* **2014**, *16*, 3059−3067.
(14) Lv, S.; Zhang, K.; Zhu, L.; Tang, D. *Anal. Chem.* **2020**, *92*, 1470−1476.
(15) Li, Y. M.; Wang, R.; Zheng, W.; Li, Y. M. *Inorg. Chem.* **2019**, *58*, 8230−8236.
(16) Liu, Q.; Xu, M.; Yang, T. S.; Tian, B.; Zhang, X. L.; Li, F. Y. *ACS Appl. Mater. Interfaces* **2018**, *10*, 9883−9888.
(17) Xu, J. T.; Yang, P. P.; Sun, M. D.; Bi, H. T.; Liu, B.; Yang, D.; Gai, S. L.; He, F.; Lin, J. *ACS Nano* **2017**, *11*, 4133−4144.
(18) Lucky, S. S.; Muhammad Idris, N.; Li, Z.; Huang, K.; Soo, K. C.; Zhang, Y. *ACS Nano* **2015**, *9*, 191−205.
(19) Li, D.; Yu, S. H.; Jiang, H. L. *Adv. Mater.* **2018**, *30*, 1707377.
(20) Luo, Z.; Zhang, L.; Zeng, R.; Su, L.; Tang, D. *Anal. Chem.* **2018**, *90*, 9568−9575.
(21) Yang, X.; Shi, D.; Zhu, S.; Wang, B.; Zhang, X.; Wang, G. *ACS Sens* **2018**, *3*, 1368−1375.
(22) Jia, Y.; Wu, F.; Liu, P.; Zhou, G.; Yu, B.; Lou, X.; Xia, F. *Talanta* **2019**, *198*, 71−77.
(23) Lu, Z.; Chen, X.; Wang, Y.; Zheng, X.; Li, C. M. *Microchim. Acta* **2015**, *182*, 571−578.
(24) Mo, R.; He, L.; Yan, X.; Su, T.; Zhou, C.; Wang, Z.; Hong, P.; Sun, S.; Li, C. *Electrochem. Commun.* **2018**, *95*, 9−13.
(25) Danesh, N. M.; Bostan, H. B.; Abnous, K.; Ramezani, M.; Youssefi, K.; Taghdisi, S. M.; Karimi, G. *TrAC, Trends Anal. Chem.* **2018**, *99*, 117−128.
(26) Wang, F.; Han, Y.; Wang, S.; Ye, Z.; Wei, L.; Xiao, L. *Anal. Chem.* **2019**, *91*, 11856−11863.

https://dx.doi.org/10.1021/acs.analchem.0c04248
Anal. Chem. XXXX, XXX, XXX−XXX

(27) Ren, M.; Xu, H.; Huang, X.; Kuang, M.; Xiong, Y.; Xu, H.; Xu, Y.; Chen, H.; Wang, A. *ACS Appl. Mater. Interfaces* **2014**, *6*, 14215−14222.
(28) An, K.; Lu, X.; Wang, C.; Qian, J.; Chen, Q.; Hao, N.; Wang, K. *Anal. Chem.* **2019**, *91*, 8660−8666.
(29) Qian, J.; Cui, H.; Lu, X.; Wang, C.; An, K.; Hao, N.; Wang, K. *Chem. Eng. J.* **2020**, *401*, 126017.
(30) Okoth, O. K.; Yan, K.; Liu, Y.; Zhang, J. *Biosens. Bioelectron.* **2016**, *86*, 636−642.
(31) Feng, W.; Zhang, L.; Zhang, Y.; Yang, Y.; Fang, Z.; Wang, B.; Zhang, S.; Liu, P. *J. Mater. Chem. A* **2017**, *5*, 10311−10320.
(32) Gao, J.; Chen, Y.; Ji, W.; Gao, Z.; Zhang, J. *Analyst* **2019**, *144*, 6617−6624.
(33) Wei, Q. X.; Wang, C.; Zhou, X.; Wu, T.; Wang, Y. Y.; Li, C. Y.; Yang, N. J. *Biosens. Bioelectron.* **2019**, *142*, 111540.
(34) Yao, X.; Gao, J.; Yan, K.; Chen, Y.; Zhang, J. *Anal. Chem.* **2020**, *92*, 8026−8030.

https://dx.doi.org/10.1021/acs.analchem.0c04248
Anal. Chem. XXXX, XXX, XXX−XXX